Damage assessment of CNT-doped composites through IR-thermography and electrical resistance measurement

Kundo Park[1,2], Seunghwa Ryu[1], Flavia Libonati[2]

Affiliations

[1]Department of Mechanical Engineering, Korea Advanced Institute of Science and Technology (KAIST), Daejeon 34141, Republic of Korea

[2]Department of Mechanical Engineering, Politecnico di Milano, Milano, Italy

Keywords

Self-sensing materials, Damage, IR thermography, Electrical resistance measurement, CNTs

Abstract

Rooted in their heterogeneous microstructure, composite materials possess high strength-to-weight and stiffness-to-weight ratios, making them essential building blocks for a wide range of industrial applications. However, their complicated microstructure makes it difficult to predict the failure mechanism and residual life under varying external loads. The in-situ health monitoring system has received much attention in recent years as one of the promising solutions for the aforementioned limitations of composite material. In this research, we suggest a coupled health monitoring system where IR thermography and electrical resistance measurement are utilized simultaneously to diagnose the damage state of the composite materials during tensile testing. The deformation and failure timeline of GFRP under quasi-static tensile loading could be subdivided into three characteristic regions, here named as damage levels, characterized by i) elastic deformation without damage formation, ii) formation of distributed micro-damages, and iii) enlargement of concentrated damage. By employing a multiphysics simulation framework, we modeled the interplay between physical phenomena occurring in three damage stages, involving crack propagation, variation in the temperature profile and electrical resistance. The results also allowed us to have an estimation of the 'damage stress(σ_D)', a value that represents the onset of micro-damage, which has a negligible effect on the elastic properties, but might be dangerous under cyclic loading.

1. Introduction

Composite materials, combination of multiple constituent materials with significantly different mechanical properties in a particular microstructure, are renowned for their outstanding strength-to-weight and stiffness-to-weight ratios. Due to their excellent mechanical properties, the use of composite materials has been rapidly increasing in diverse industries, such as aviation, automotive, and construction, replacing the conventional homogeneous materials. However, the heterogeneous nature of its microstructure not only resulted in its unique mechanical property, but also made it more difficult to predict its failure mechanism and residual material life under fatigue loading. Due to their microstructural complexity, composite materials exhibit various failure mechanisms such as fiber rupture, interfacial debonding, and matrix cracking, depending on the type of load applied and the material microstructure. Especially for the mechanical components that have to endure cyclic loads, which is a common application of composite materials, the prediction of material's residual life remains an open question. Consequently, in safety-critical applications of composite materials, such as aircrafts and buildings, the structures are often 'overdesigned' to ensure high safety margin against unexpected failure, thus not effectively exploiting their lightweight potential.

The in-situ health monitoring system has received large attention in recent years as a promising solution for the aforementioned limitation of composite material [1]. In order to avoid overdesign, damage, and defects evolving in the material, the microstructure must be evaluated through the health monitoring system on a regular basis so that preventative measures can be taken prior to the failure [2]. Various non-destructive testing techniques, such as ultrasonic analysis, radiographic analysis, and IR-thermography, are adopted for structural health monitoring of materials [3]. A recently proposed in-situ health monitoring techniques is the damage analysis by electrical resistance measurement [4-6]. As depicted in the **Figure 1.a-b**, one can form an electrically conductive network in a non-conductive composite material by dispersing carbon nanotubes (CNTs) during the material manufacturing stage. By evaluating the change in the electrical resistance of this CNT percolation network, which depends on material deformation and internal micro-defects, it is possible to evaluate the onset and evolution of micro damage in a composite specimen, which cannot be detected from stress-strain curves. The applicability of this technique for material damage sensing has been shown in various previous studies, and it was highlighted that this methodology is particularly effective for detecting the initiation of permanent damage [6-8]. However, the electrical resistance value

does not provide any information about the spatial distribution of damage in the specimen. Such limitation can be complemented by coupling another nondestructive method [7].

In the present study, we demonstrate a coupled non-destructive health monitoring method by employing both infrared (IR) thermography [9,10] and electric resistant measurement. Various thermo-mechanical phenomena, such as thermoelastic effect, evolution of micro-defects, and fiber-matrix delamination can occur inside a material under deformation and fracture, inducing a spatiotemporal variation of the temperature. The surface temperature of a material body can be analyzed in a non-contacting manner by IR-detection using a thermal camera. The varying temperature distribution measured by the thermal camera can be used to locate the evolution of damage in the material (**Figure 1.c-d**), which is a unique advantage of employing the IR-thermography [10]. To deepen our understanding on the interplay between damage evolution (e.g. micro and macro crack), temperature profile, and electrical resistance change, we employ multiphysics crack phase field simulation that not only captures elastic deformation, crack initiation and propagation, but thermo-mechanical phenomena and electric conduction as well.

The coupled health monitoring system, where IR thermography and electrical resistance measurement are simultaneously used, aim to diagnose the damage state of the composite materials. During a uniaxial tensile test of GFRP (glass fiber reinforced polymer), we identified different damage levels and carried out interrupted tensile tests until different levels of induced damage. We then complemented our experimental study with multiphysics simulations, which offers valuable insights into the multiphysics nature of the phenomena involved. The deformation and failure timeline of GFRP under quasi-static tensile loading could be subdivided into three characteristic regions, here named as damage levels, characterized by i) elastic deformation without damage formation, ii) formation of distributed micro-damages, and iii) enlargement of concentrated damage. Based on the results, we estimated the 'damage stress(σ_D)', a value that indicates the onset of micro-damage, which has negligible effect on the elastic response, and thus cannot be identified solely from stress-strain curves. Yet, it may be dangerous under cyclic loading.

2. Materials and methods

2.1. Experiment

2.1.1. Material design and fabrication

In the present study, we consider a multiscale CNT-doped Glass Fiber Reinforced Plastic (GFRP) material made of a bi-component Epoxy matrix (Araldite® LY 556, by Huntsman) mixed in 100:23 ratio with hardener (XB 3473, by Huntsman) and reinforced by E-glass fibers (GF EBX600 supplied by Selcom) layered in a symmetric and balanced stacking sequence $[0^\circ/45^\circ/90^\circ/-45^\circ]_{2S}$. The epoxy matrix is doped with Nanocyl NC 700 multiwall carbon nanotubes (diameter 9.5 nm and length up to 1.5 μm) to form a conductive network in the microstructure. MWCNT/epoxy mixtures were manufactured by three-roll milling, using an EXAKT 80E mini calendar. The amount of CNTs was set to 0.1% wt., as it has proven to ensure a good electrical sensitivity and is not far from the percolation threshold [15]. After the mechanical dispersion of CNTs, a degasification step was carried out at 80 ºC for 15 minutes, to remove the air entrapped in the mixture. The hardener was added to the mixture, then injected into a GF preform. Multiscale GFRP plates were manufactured by Resin Transfer Molding (RTM) technique, where the MWCNT/epoxy mixture was injected at a constant pressure (2 bar) and temperature (80 ºC), to facilitate the infiltration process, then cured for 8 h at 140 ºC.

2.1.2. Sample preparation

The material was cut into 16 rectangular specimens having identical shape shown in **Figure 2.b, 2.c** (L=225mm, w=25mm, s=50mm, a=15mm, t=3mm). Abrasive waterjet machine was used to cut the specimens, resulting in high dimensional tolerance and consistent cut surface quality throughout the 16 specimens cut. The dimensions were chosen according to the ASTM D3039/D3039M standard [16]. Tabs were glued onto the specimen ends using a 3M Scotch-Weld Epoxy Adhesive DP100 in order to promote a correct load transfer and prevent undesired fracture in the grip area during the tensile test. The tabs are made of an insulating material (polycarbonate) to provide an electrically insulated layer between the specimen and the tensile testing machine. To ensure a perfect insulation of the sample from the tensile test machine, insulation tape was also wrapped around the grip part of the specimen. Finally, two electrical connections were built onto each end of the sample, forming robust adhesions between the sample surface and electric wires by means of aluminum foil tape and silver conductive paint.

2.1.3. Experimental testing setup

Uniaxial tensile tests of GFRP specimens were performed on a universal tensile testing machine (MTS Alliance RT100 equipped with 150 kN load cell), in displacement control mode, with 2mm/min crosshead speed, and 10Hz data sampling frequency. During the tensile tests, the flat surface of the specimen was scanned with an IR camera to monitor and record the surface temperature variation during tensile loading, according to the testing setup shown in the **Figure 2.a**. The thermal camera used is FLIR Titanium, which is capable of detecting middle wave infrared range (MWIR) between 3 and 5μm wavelength with 25mK thermal sensitivity. 25Hz sampling frequency was used to acquire the thermal data and post-processing of the data was performed with ALTAIR, a temperature field mapping software, for detection of the damaged zone. To monitor the electrical resistance of the specimen during the tensile test, an electrical setup that functions as a voltage-current meter was built with the current generator, power supply, digital-multimeter, and NI DAQ board as key components. During the test, the resistance R of the specimen was monitored by performing a simple calculation according to the Ohm's law, R=V/I. Here, constant current I is sustained by the current generator and the electrical potential difference V between the two nodes on the specimen was tracked with NI DAQ system. The High frequency noise in the acquired electrical signal is filtered with Savitzky-Golay filtering function (sgolayfilt) in MATLAB. From now on, the above described material testing setup will be called as 3-channel tensile testing, as it simultaneously tracks thermal, electrical, and mechanical behavior during a uniaxial tensile test.

2.1.4. Uniaxial tensile tests

The aforementioned 3-channel tensile tests were performed on 7 GFRP specimens. From this test, three resultant curves (variation of stress, temperature, and electrical resistance vs. strain) were obtained simultaneously for each sample. These uniaxial tensile tests were conducted to compare the output from three channel measurements and to see how they represent the internal damage evolution inside the material during the material's failure process.

2.1.5. Interrupted uniaxial tensile tests

Based on mechanical, thermal, and electrical signals measured from the 3-channel tensile tests, we identified three characteristic 'damage levels', corresponding to characteristic stress ranges. To understand the internal damage state of the material in each of the damage

levels, we performed interrupted static tests, in which the material is loaded until reaching a predefined load level and then completely unloaded. The specimens were loaded up to three different loads, corresponding to representative stress levels of 53MPa, 120MPa, and 147MPa, chosen to be within Damage Region I, II, and III, respectively (see **Figure 3**). These stress levels were chosen after performing an initial experimental campaign of tensile testing. Two types of interrupted tensile tests were performed in this study: (i) single loading-unloading cycle and (ii) double loading-unloading cycles.

In the single loading-unloading test, the specimens that experienced different damage levels were cut after the test and the cross sections were analyzed by SEM (Scanning Electron Microscope) to assess the damage state in the material. In the double loading-unloading cycle tests, new specimens were tested under repeated loading-unloading cycles with various maximum loads while monitoring the internal damage evolution via mechanical (stiffness reduction), electrical (permanent electrical resistance change), and thermal (temperature variation map) signals. In each loading cycle, the stiffness was determined from the linear fit on the initial part of the stress curves. The stiffness reduction $D_{stiffness}$ were evaluated as shown in **Eq. 1** to understand the damage evolution in the material.

$$D_{stiffness} = \frac{E_1 - E_2}{E_1} \qquad \textbf{Eq. 1}$$

The subscripts 1 and 2 in Eq. 1 indicate 1st and 2nd loading unloading cycle, respectively. Secondly, the permanent change in the electrical resistance after the 1st loading cycle was evaluated, by monitoring the evolution of the resistance during two cycles. This analysis was conducted because the residual electrical resistance after the 1st loading cycle accounts for the permanent damage evolution inside the material. Finally, a qualitative analysis of the material's temperature variation during its deformation and fracture process was performed. The expected outcome of this series of damage analysis is to understand the physical phenomena that occur in each damage level, and also characterize corresponding spatiotemporal internal damage evolution in each damage region.

2.1.6. Microscopic analyses

For the SEM analysis, the cross sections of the cut specimen were thoroughly polished with various circular sandpapers (grit number of 100, 180, 320, 600, 1000) using disc polishing machine in order to remove micro-scratches on the cut surface. Then, further polishing process was conducted by applying diamond compound abrasive onto the disc polishing machine. The

polished surface is then gold-sputtered, and finally analyzed by SEM (Carl ZEISS EVO 50 model). SEM images were captured by both backscattering and secondary electron methods in order to better spot the internal damage. Through SEM analysis, we observed and compared the microstructure of specimens that experienced loading-unloading cycle of different damage levels.

2.2. Multiphysics modeling

2.2.1. Multiphysics simulation platform development

To deepen our understanding on the interplay between mechanical, electrical, and thermal responses of the materials, we developed a Multiphysics simulation framework that can model not only the mechanical fracture of materials, but also the electrical and thermal response during the fracture. The developed simulation platform is able to model the 3-channel tensile test of a simplified GFRP model.

In order to model the crack initiation and propagation, we implemented three-dimensional phase-field algorithm in the commercial FEM solver Abaqus/Standard through User Element (UEL) function based on a hybrid formulation, which is shown to be adequate for modeling curvilinear crack growth in composite materials [23]. The phase-field is a scalar variable—between 0 and 1—that represents the damage state of each element. The phase-field is updated in every iteration of the simulation, based on the mechanical stress distribution in the previous iteration step. If its value reaches 1, the material element is considered fully broken and its stiffness and stress are reduced to zero. This means that that the broken element completely loses its load bearing capacity. The merit of adopting a phase field approach is that it can simulate the curvilinear fracture paths, branching and even crack coalescence, not requiring any predefined crack paths, thus overcoming the limitation of other numerical techniques (e.g., cohesive elements and XFEM).

To simulate the electrical response of the material under deformation and fracture, we added an electrical conduction simulation to the aforementioned phase field model [26]. Two governing equations of quasi-static electrical conduction, Ohm's law and Maxwell's conservation of charge, were combined into a single FEM matrix equation, and the corresponding algorithm code was added to our phase field UEL code. To capture the increase of the electric resistance upon growth, we introduced the concept of electrical conductivity degradation such that the electrical conduction does not occur across the cracked region in the

material. We assume that the electrical conductivity of an element linearly decreases to zero until the phase value reaches 0.9 and stays zero upon further increase of the phase value.

Thermo-mechanical phenomena were modeled by coupling the local temperature field with the stress state at the corresponding position, and adjusting the thermal conductivity by the phase value. First, to model the time dependent heat conduction in the material, we combined the two governing equations of thermal conduction, Fourier's law of heat conduction and conservation of heat equation, into a unified FEM equation, and the corresponding fortran UEL code was applied to the phase field model [27]. The thermal conductivity linearly decreases with increase of the phase value, as is the case for the electrical conductivity. Secondly, thermoelastic effect was taken into account: a thermo-mechanical phenomenon where the temperature of material changes upon elastic deformation [28]. This negative linear relationship between temperature and mechanical stress induces a homogeneous temperature reduction in the material when it experiences a tensile deformation, and vice versa. Lastly, we modeled the friction heat generation near the crack at the instant of crack nucleation and propagation, by applying the corresponding amount of heat to the elements at the instant of their phase value reaching 0.9.

2.2.2 Virtual GFRP specimen design and simulation conditions.

Two-dimensional uniaxial GFRP specimen was designed in Abaqus for multiphysics tensile test simulation (**Figure 7.a**), which is designed to visualize the complex interplay between crack initiation and propagation, electric conductance over the sample, and temperature profile. Similarly to the real GFRP specimen used in the experiment, E-glass fiber was chosen as reinforcement material and epoxy resin was chosen as the matrix. Inside the epoxy matrix, 40 glass fibers with random radius are dispersed in a random manner. A fine mesh was constructed over the specimen model by choosing an element size of $l \cong 0.01\text{m}$. As a result, a three-dimensional uniaxial GFRP specimen with 63571 linear brick elements was prepared for the simulation. **Table 1** shows the material properties required as input parameters for the multiphysics simulation [29, 30]. The top surface of the specimen was pulled upwards with a step displacement size of $\Delta u = 1.4 \times 10^{-3} m$ while the bottom surface was fixed in the loading direction. 100V and 0V of electrical potential was set at the top and bottom surface of the specimen, respectively as electrical boundary conditions. The initial temperature of the specimen is set as 300K and the specimen is in an adiabatic condition.

3. Results and Discussion

3.1. Experiment

3.1.1. Uniaxial tensile tests

Seven identical GFRP samples were examined via the 3-channel tensile test. **Figure 3** represents the mechanical stress, average temperature change, and electrical resistance change of GFRP samples as a function of tensile strain during a uniaxial tensile test. Based on the deformation and failure process of the CNT-doped GFRP we could identify three characteristic regions, corresponding to three damage levels. The results from the seven tests showed both qualitative and quantitative repeatability in that the three characteristic damage levels were clearly identified through the graphical analysis and they were similar in all seven trials.

Damage Level I:

The first region is characterized by a completely elastic behavior of the material. Both the fiber and matrix undergo linear elastic deformation where all the mechanical input energy is elastically stored by the composite. Under the linear elastic deformation mode, the temperature of the specimen is primarily affected by the thermoelastic effect, a negative linear relationship between the stress state of a homogeneous isotropic material in adiabatic conditions and its temperature variation [28].

$$\Delta \mathrm{T} = -\frac{\alpha}{\rho C_p} T_0 \Delta\sigma \qquad \textbf{Eq. 2}$$

Where α is the coefficient of linear thermal expansion, ρ is the density, C_p is the specific heat, T_0 is the initial temperature of the body, and $\Delta\sigma = \Delta(\sigma_1 + \sigma_2 + \sigma_3)$ is the variation of the first stress invariant[2]. As it can be understood by the relationship, the temperature of the body decreases linearly with the applied stress. On the other hand, the electrical resistance trend shows a negligible change in this damage level because the microstructure of the specimen does not possess any permanent damage and thus, the CNT conductive network built inside the material is not structurally altered.

Damage Level II:

The second region still shows smooth stress-strain curve and thus can be considered as an elastic regime that does not involve the formation of permanent damages, if two other

channels are not available. Interestingly, the average temperature in this regime starts to deviate from the linear response, and decreases nonlinearly until it reaches the minimum. The temperature still shows a decreasing trend due to the tensile thermoelastic effect but, in addition, local heat generation is induced in the material due to the formation of distributed (or well dispersed) micro-damages (**Figure 4.a**). Also, the local stress relaxation around the damage leads to the increase of the temperature around it. In addition, some damage processes, such as fiber-matrix debonding and slippage may have caused heat due to mechanical friction. On the other hand, the electrical resistance suddenly starts to rise in this region due to permanent damage formation. The micro-defects can form several insulating zones in the CNT percolation network, thus increasing the overall electrical resistance of the specimen.

Damage Level III:

In the third region, nonlinear mechanical response is observed and the energy is gradually released while the damage macroscopically propagates until failure. In this stage, upon further increase of the mechanical loading, many existing micro-damages evolve into a few macroscale cracks, and one or two cracks propagate through the entire sample. The heat generation due to this significant damage evolution prevails over the temperature-reducing thermoelastic effect, thus the temperature started to increase in this level. Depending on the type of failure, an initial damage localization and local temperature increase may occur, followed by a damage growth and spread throughout the samples and a general rise in temperature. The electrical resistance of the specimen in this damage level continues to increase, as the macroscale crack induces significantly large electrical insulation zone in the material. When the complete fracture occurs in the specimen, the CNT network in this stage can no more function as a conductive medium, and the electrical resistance reaches the saturation value.

3.1.2. Interrupted static tests

i) Single loading-unloading cycle

To better characterize the damage evolution at each damage level, the specimens loaded to various damage levels were cut and the cross-sections analyzed by SEM as shown in Figure **5**. The microscopic images show that no damage was created in the first region (**Figure 5.a**). The magnified image illustrates some micro-voids in the fiber section, which are undesired defects originated during the manufacturing process. In the specimen that reached

the second damage level, fiber-matrix detachments were initiated and resulted in a local irreversible crack growth (**Figure 5.b**). In the third damage level, the material experienced critical crack growths in a global manner (**Figure 5.c**). Macroscopic crack propagations affect both the magnitude and distribution of concentrated stresses, which will cause the fast fracture of the specimen. Based on the comparison between **Figure 5.a** and **Figure 5.b**, one can conclude that the damage stress value represents a threshold for damage initiation. The damage originated at this level does not significantly affect the elastic response (which is determined by the average elastic energy of the entire specimen), but may be dangerous under cyclic loading, i.e. worsen the fatigue behavior of the material. The threshold stress is known to be correlated with the fatigue strength [9,13,14].

ii) Double loading-unloading cycles

A quantitative evaluation of damage in the specimen was possible by double loading-unloading tests. The stress, temperature, and electrical resistance trends of a sample under double loading-unloading tests at various load levels are shown in **Figure 6.b**.

a. Mechanical perspective: Stiffness degradation

Figure 6.a represents the stiffness changes from the double loading-unloading tests of damage level I, level II, and level III, respectively. Stiffness reduction of a material is one of the indicators that represent the internal damage evolution in the composite material [31,32]. The evolution of damages in the internal structure, especially those oriented and growing orthogonally to the loading direction, makes the composite material more vulnerable to the deformation under external loads.

As the first damage level is characterized by linear elasticity, stiffness reduction did not occur in this double loading-unloading condition. Indeed, the material experienced 1.46% of increase in stiffness instead, which can be originated from an artifact from the measurements. Indeed, the stiffness was determined considering the strain calculated from the crosshead displacement and not from a local measurement by means of an extensometer. The latter was not adopted in the tensile tests, to avoid any interference with the electrical circuit. The absence of a stiffness degradation indicates that the material only experienced a reversible linear elastic deformation and thus, no permanent damages were form in this damage level. In contrast, the stiffness reductions were clearly seen in the tests interrupted at the second and third damage level. When the sample experienced the loading cycles of second damage level, 1.11% of

stiffness degradation occurred, which indicates the permanent damage initiation in the composite microstructure. Moreover, the third phase was characterized by a further stiffness degradation of 2.08%, which corresponds to a macroscopic damage growth right before the failure. The stiffness degradation is limited in spite of macroscopic damage propagation, because the stiffness is mainly governed by the longitudinal fibers. The rupture of a longitudinal fiber requires large energy and it generally precedes the final failure. Matrix microcracking, debonding and delamination mainly affect the material strength, toughness, and the fatigue properties (e.g. static strength).

b. Electrical perspective: Permanent electrical resistance change

The electrical resistance variation of the GFRP enables us to monitor the microstructural damage state during the loading and unloading cycle, as it can be seen from the blue curves in **Figure 6.b**. In the test carried out up to the first damage level, the electrical resistance signal showed negligible variation as the material experiences linear elastic deformation without any permanent damage initiation. In addition, the electrical resistance perfectly recovers back to its initial value after it is completely unloaded, meaning that the state of the material after the process is the same as its initial undamaged condition.

In contrast, the electrical resistances from the double loading-unloading tests with the stresses in the second and third damage levels shows different behaviors. In these phases, the electrical resistance shows a sudden increment after the damage stress point, indicating the onset of the permanent damage formation. Moreover, the electrical resistance does not recover to its initial value even after the specimen is completely unloaded; the permanent fractional electrical resistance changes are around 0.1% and 0.17% in second and third damage level loadings, respectively. In contrast with the linear elastic material behavior under the first damage level, the residual electrical resistance change, in second and third damage level regions, indicates permanent damage formation during the loading and unloading cycles.

We also note a slight reduction of electrical resistance that occurs during the unloading process. This reduction is not a result of crack healing, but it is due to crack closure. As the external tensile load is removed gradually, the contraction of the specimen body closes the internal microcracks, creating electrical contacts. During subsequent re-loading of the damaged specimen, applied tensile load causes the closed cracks to re-open elastically without any additional damage accumulation.

c. Thermal perspective: Thermal image analysis

During the loading process of the GFRP specimen, the temperature of the material varies both locally and globally due to multiple thermomechanical phenomena that take place simultaneously in the material, as shown in **Figure 6.c**. With the aid of IR thermal camera, the deformation and fracture process of the material can be analyzed visually by monitoring the temperature variation of the specimen. For the small deformation regime in the first damage level, the temperature of the whole specimen decreases homogeneously. This global temperature reduction occurs due to the thermoelastic effect over the whole specimen body. Smooth variation of temperature is observed because the average stress and thermoelastic coefficients of glass fiber and polymer matrix are different, and the magnitude of thermoelastic effects can be different for each phase. Still, abrupt local temperature jump was not found anywhere in the temperature map, meaning the absence of permanent damage formation.

However, with the further increase of external loading, the material reaches its second damage level, numerous local temperatures jump spots appear and disappear as if bright spots blink all over the specimen, in addition to the global temperature reduction trend continued from the first damage level. The local temperature jumps observed in this phase are responsible for the onset of the permanent micro-damages in the examined material. At damage onset in the material, local temperature rise occurs due to thermoelastic effect, local stress relaxation upon micro-crack opening, and the frictional heat diffusion near the damage formation spot.

Finally, when the specimen reaches its third damage level, the local temperature jump spots seen in the second phase are not observed as frequently. Instead, significant temperature rise occurs in several spots and noticeable temperature rise is maintained during the tensile deformation. These spots accompanying high temperature rise are associated with the macroscale damage growth. Since the stress concentration is intensified with the damage size, continuous heat generation follows due to the local stress relaxation induced thermoelastic effect and the frictional heat diffusion. We note that the composite material in the third damage phase is in a structurally critical state, just prior to the catastrophic crack propagation.

3.1.3 Estimation of Fatigue strength

Based on the three characteristic regions and damage levels defined in the resultant graphs (**Figure 3**), it was possible to evaluate the damage stress (σ_D) of the studied material. We define the damage stress as the threshold stress value dividing the first damage level and

the second level. This is the point when the material starts to lose its linear elastic deformation behavior and the first irreversible micro-damage evolution begins in the material. With this understanding of material deformation characteristic before and after the damage stress point, the material behavior under fatigue loading can be deduced, based on previous literature studies [14]. If a material undergoes a cyclic load that triggers a peak stress lower than the damage stress of material, the material will experience reversible loading-unloading process without onset of internal damage. However, if the cyclic load leads to a peak stress higher than the damage stress of the material, micro-damage will be accumulated in every cycle and the material will end up in a fatigue failure. In this perspective, the material damage stress evaluated in this paper can represent the fatigue strength of the studied material.

In the S-N curve of a single metal material, it is possible to define the endurance limit, which is an important fatigue property of material: the amplitude of cyclic stress that can be applied to the material without causing fatigue failure. However, composite materials, such as GFRP, do not have a distinct limit and will eventually fail even in a small amplitude stress cycle. Therefore, a different design approach had to be used. In these cases, the terminology 'fatigue strength' is used to characterize the important stress threshold where a significant inflection occurs the in S-N curve. Previous studies showed that the damage stresses of various materials, evaluated through IR thermography, showed a good agreement with the actual fatigue strengths [13,14]. From this research, the 3-channel tensile testing method was applied onto 7 identical GFRP specimens and it was possible determine the damage stress value both precisely and repeatably; the damage stress values were within the range of 81 ± 3 MPa in all 7 trials.

3.2. Multiphysics modeling study

By employing the multiphysics simulation platform, we simulate the deformation and fracture behavior of 2D GFRP composite material under uniaxial tensile test. The interplay between mechanical, electrical, and thermal behaviors of the GFRP specimen during the tensile deformation are captured in various instances and collected in **Figure 7.b**. Also, the **Figure 8** illustrates the 3-channel trends of the specimen during the simulation: stress, electrical resistance and temperature of the specimen.

From the phase field results in the **Figure 7.b**, which represents the damage field within the material, it can be observed that the material showed a linear elastic deformation

mode in its early deformation stage. The randomly dispersed glass fibers result in the inhomogeneous stress distribution within the material, inducing significant stress concentrations in particular locations. This inhomogeneity makes the material volume in the stress concentration zones to reach a higher phase level earlier, or forming small scale damages. As soon as the phase of some elements reached a value of 1 due to the prominent stress concentration, a rapid crack propagation was initiated. The nucleation of large-enough crack is subsequently followed by a rapid crack growth along the entire cross section of the specimen.

The electrical current density field map in **Figure 7.b** illustrates the path of electrical current that flows from upper surface of the specimen to the bottom. The electrical conduction mainly occurs in the locations of a high electrical current density value represented by the green to blue color spectrum. On the other hand, the current does not flow through the red and yellow region due to insulating glass fibers. In the stage of linear elastic deformation, the overall electric current field does not change as the microstructural geometry of the specimen is not altered. Consequently, the electrical resistance curve undergoes very small change originated from the overall elongation of the sample (consequently, longer electric path) due to the tensile loading. The crack is introduced, the electrical current field starts to change abruptly as the current cannot pass over the crack. The rapid crack evolution causes a bottleneck in the current path and a dramatic increase in the electrical resistance of the overall domain is seen in the graph.

The temperature field decreases in an inhomogeneous manner during the elastic deformation as the temperature change within the material in this stage is solely induced by the changing stress field, which is non-uniformly intensified. The thermoelastic effect triggers a greater temperature reduction at a location where the stress concentration occurs, and such regions can be readily noted in the temperature map in **Figure 7.b**. As the crack is nucleated at the highest stress region, the temperature of the elements near the crack increased due to the relaxation of stress resulting in a thermoelastic temperature rise. In addition, the frictional heat modeled in this multiphysics simulation provided extra heat to the completely broken elements and the heat is diffused throughout the entire specimen, starting from the nearest elements. As the crack evolves rapidly, the elastic energy stored in the material is released and the regions, where stress relaxation occurs, recover its original temperature: 300K.

4. Conclusion

In the present study, we monitor the failure process of a CNT-doped GFRP in uniaxial tensile tests by coupling an electrical resistance measurement and an IR thermography. The electrical resistance and temperature data obtained in the 3-channel tensile test allows us to examine the micro-damage evolution that cannot be observed solely from the mechanical response. Additionally, the stress value that corresponds to the transition from the first damage level to the second damage level was defined as 'Damage stress', which we believe correlate strongly with the fatigue strength of the material.

To better understand the physical phenomena occurring in the material microstructure at each of the three damage levels, single loading-unloading tests and double loading-unloading tests were carried out. From the single loading-unloading tests, the specimens in different damage level phases were cut and the cross sections were analyzed with SEM. In the double loading-unloading tests, different damage parameters such as stiffness degradation and permanent electrical resistance change were evaluated for each of the damage levels. In addition, qualitative analysis of the material's failure process was possible by analyzing the material's temperature variation filmed by IR camera during the tensile tests.

The multiphysics simulation enabled us to understand mechanical, electrical, and thermal behavior of microscopic composite structure at the instant of crack nucleation and the propagation. Electrical and thermal components were added to the crack phase field algorithm in order to model not just the mechanical fracture of composite material, but the electrical and thermal response as well.

From the results of the tests and simulations carried out, the physical state of the material microstructure in each of the damage phases were understood. In conclusion, each of the three damage levels, Level I, Level II, and Level III, were characterized by the material's initial linear elasticity, onset of micro damage evolution, and macro-scale damage propagation, respectively. Accordingly, the damage stress value of the material represents the end of material's linear elastic deformation and, at the same time, onset of permanent micro-damages. According to previous studies, the damage stress, here determined by means of two techniques, could correspond to the fatigue strength of the material as irreversible damage accumulation in the material occurs at a cyclic loading with the peak stress higher than the damage stress.

Coupled electrical resistance measurement and IR thermography monitoring technique

is therefore proposed as an effective and efficient technique capable of quickly and accurately assess the material damage, also providing an estimation of the damage stress (σ_D) of the composite, which is a reasonable estimation of the material's fatigue strength.

Tables

	Epoxy resin *matrix*	**E-glass fiber** *reinforcement*
Elastic modulus (E) [GPa]	3.2	79
Poisson's ratio (ν)	0.35	0.22
Surface energy release rate (g_c) [J/m^2]	92	10
Electrical conductivity (σ) [S/m]	0.046	0
Thermal conductivity (κ) [W/Km]	0.17	1.3
Density (ρ) [kg/m^3]	1200	2600
Specific heat capacity (c) [J/kgK]	1100	800
Linear thermal expansion coefficient (α) [K^{-1}]	55×10^{-6}	8.5×10^{-6}

Table 1. Material properties of the matrix and reinforcement used for the Multiphysics simulation.

Figures and captions

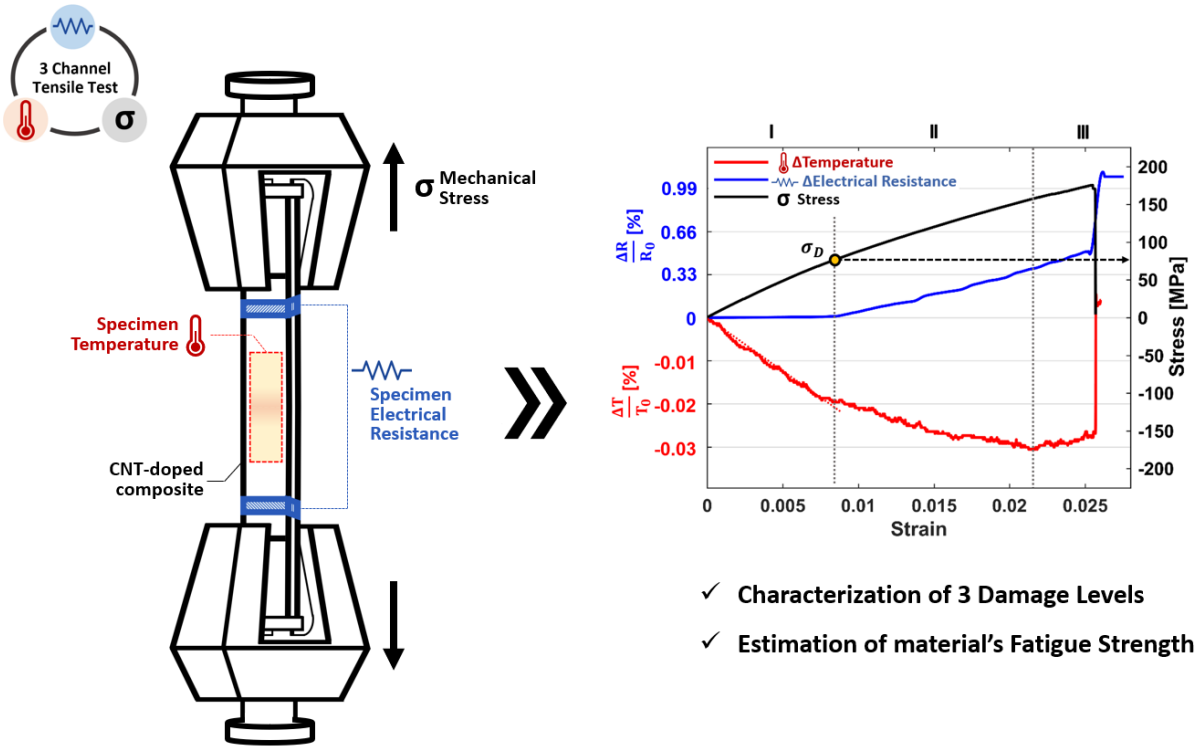

Graphical abstract. Damage assessment of a CNT-doped composite material through 3-channel tensile test.

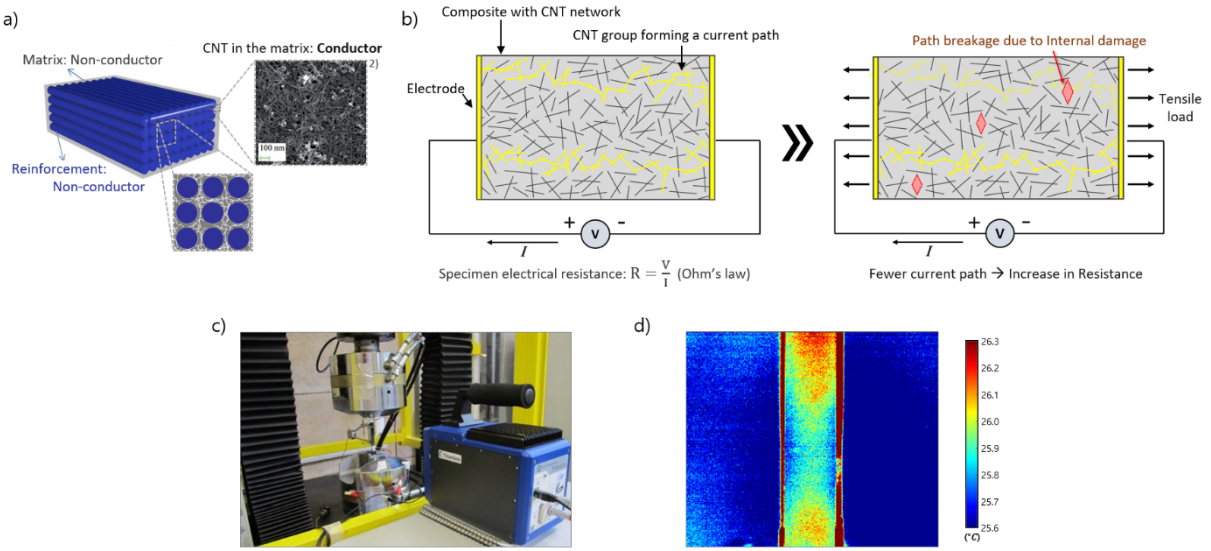

Figure 1. Material damage sensing by electrical resistance measurement and IR thermography. (a) Self sensing material - electrically conductive network of carbon nanotubes in the matrix. (b) Schematic diagram of electrical resistance measurement as a damage sensing technique. (c) Application of Infrared camera in tensile tests. (d) Thermal map of a material acquired by IR camera.

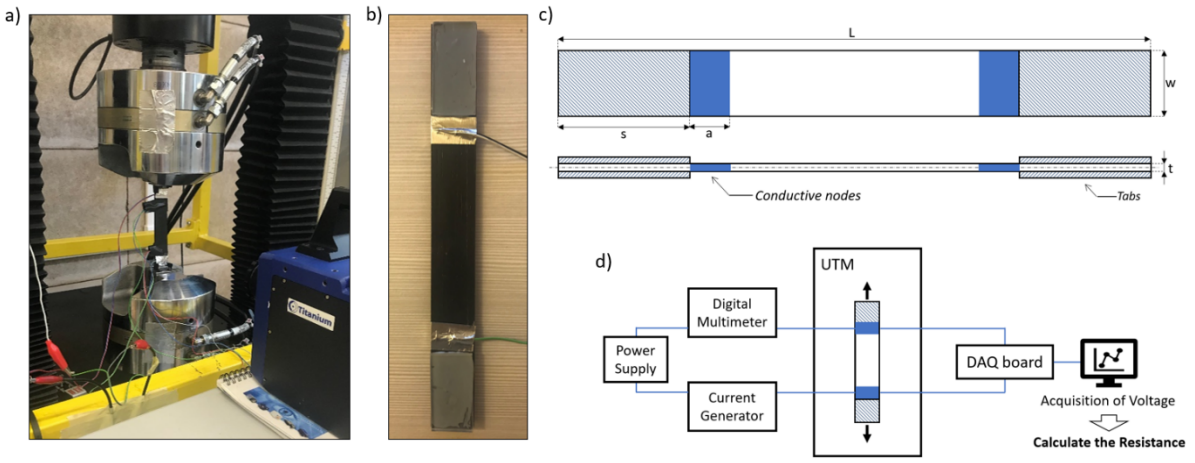

Figure 2. Experiment setup and the tested material. (a) Setup of the 3-channel tensile test. (b) CNT-doped GFRP specimen with electrical connections. (c) Specimen dimension based on ASTM D3039. (d) Circuit diagram of an electrical resistance measurement.

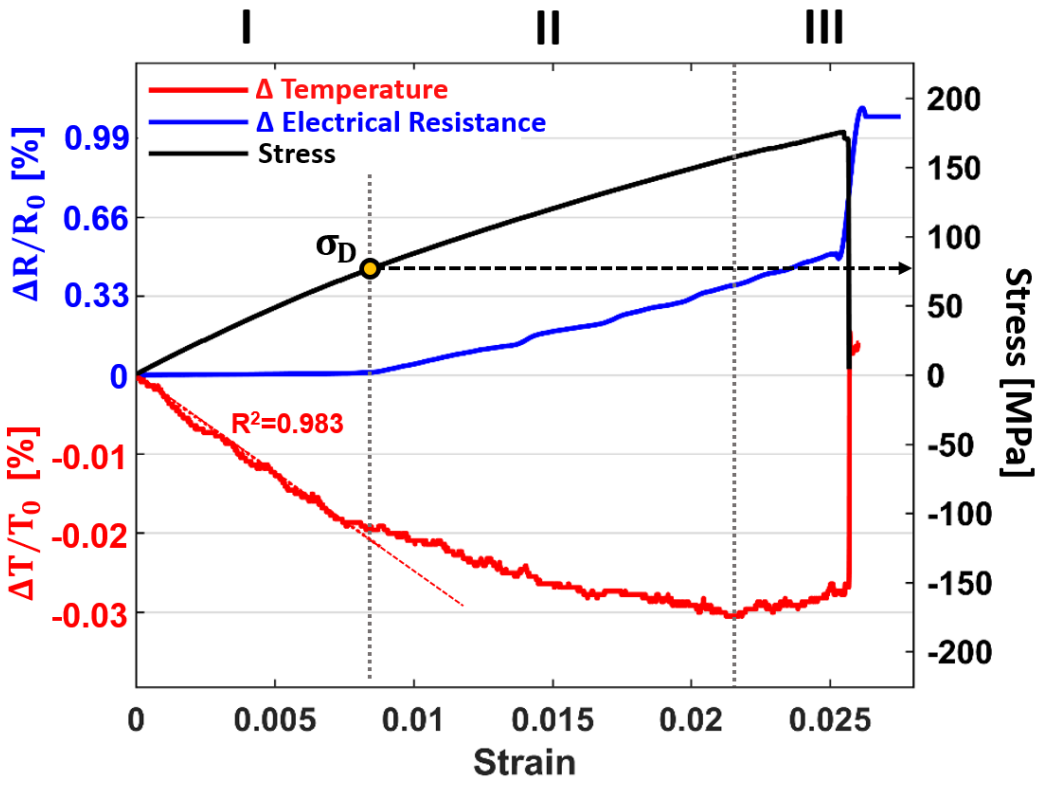

Figure 3. Result of the 3-channel tensile test on GFRP composite specimen.

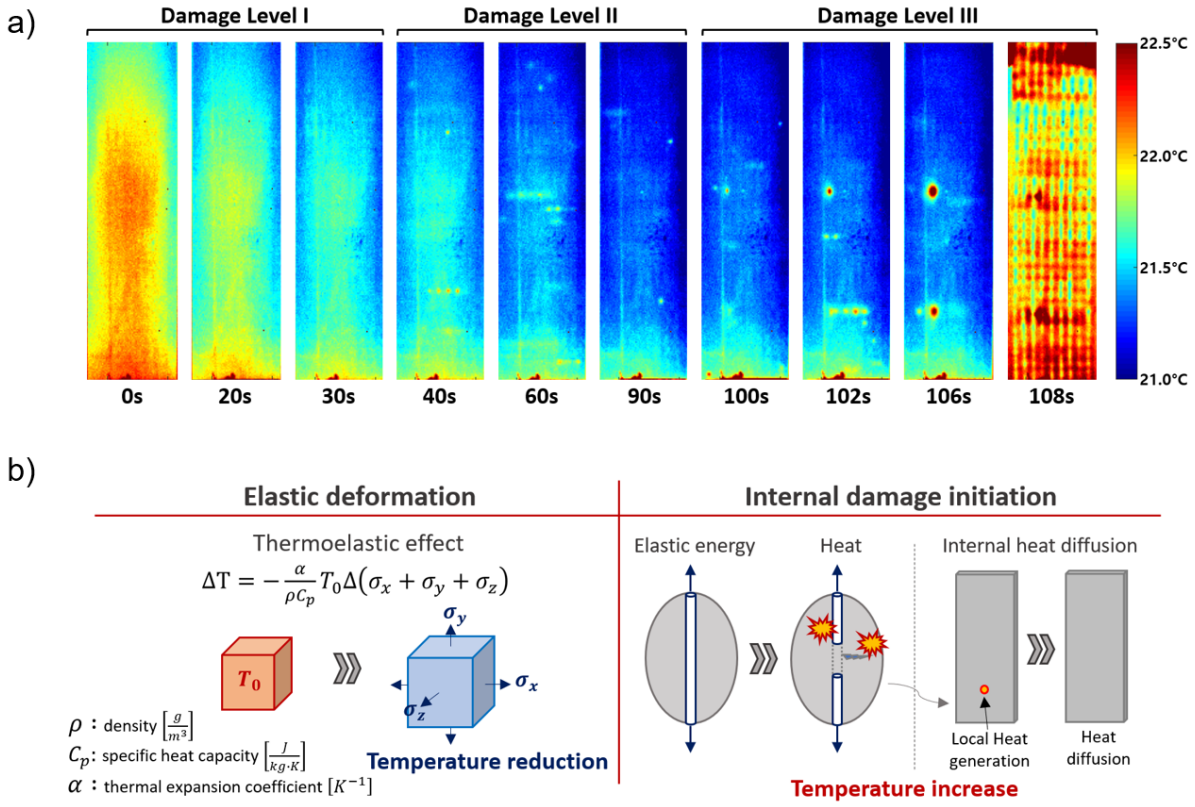

Figure 4. Thermal response of the GFRP specimen under deformation. (a) Thermal maps taken in different instants during a tensile test. (b) Key mechanisms that cause the temperature variation.

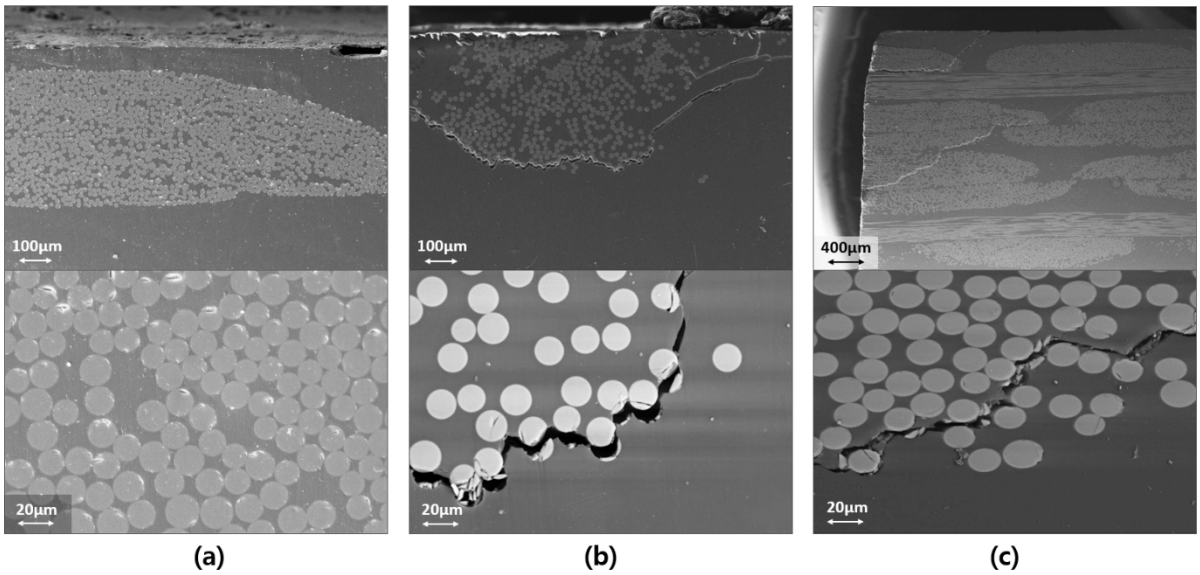

Figure 5. SEM images taken after the interrupted static tests. (a) Damage level I - peak stress: 53MPa. (b) Damage level II - peak stress: 120MPa. (c) Damage level III - peak stress: 147MPa

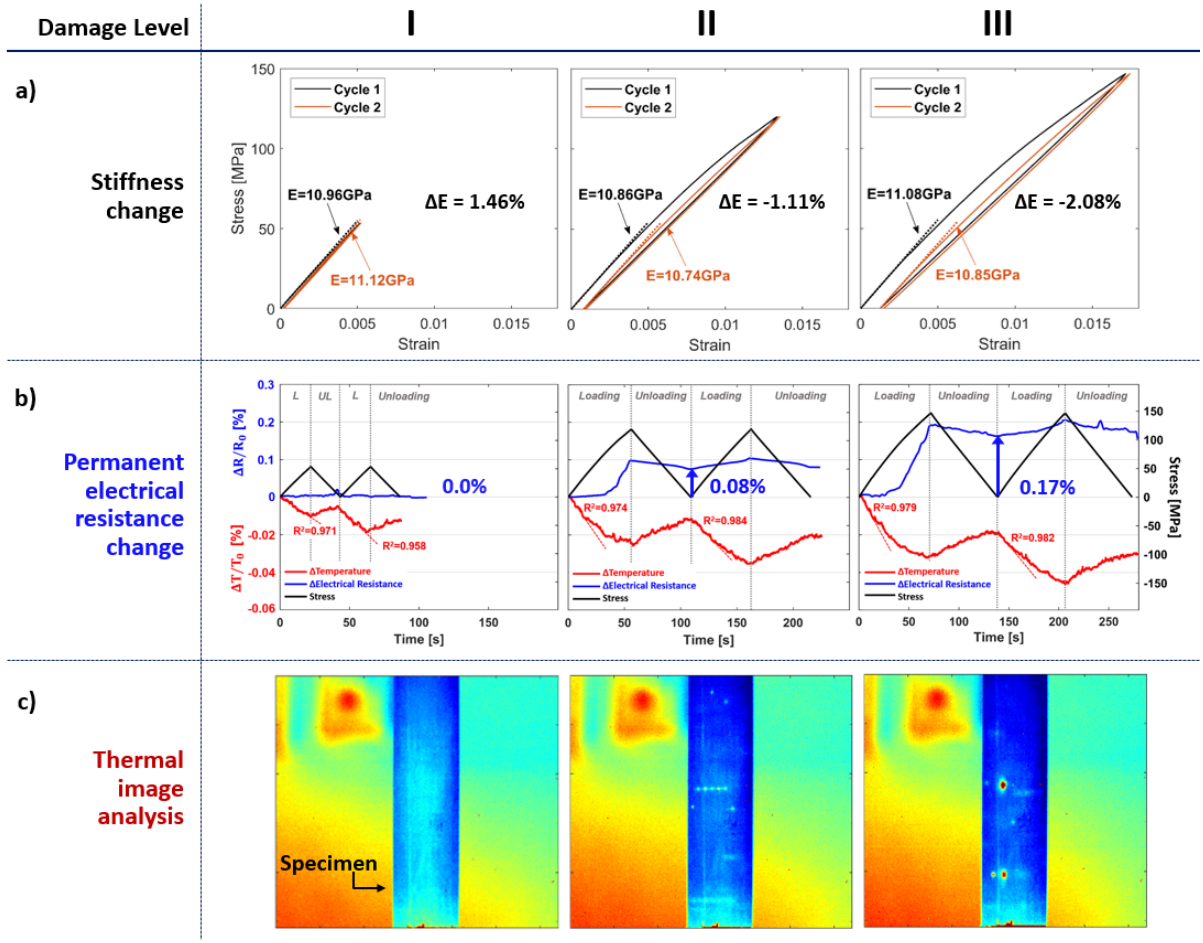

Figure 6. Mechanical, electrical, and thermal analysis on the results from interrupted static tests. (a) Stiffness degradation due to damage formation. (b) Permanent electrical resistance change induced by damage formation. (c) Analysis of the thermal image in different damage level.

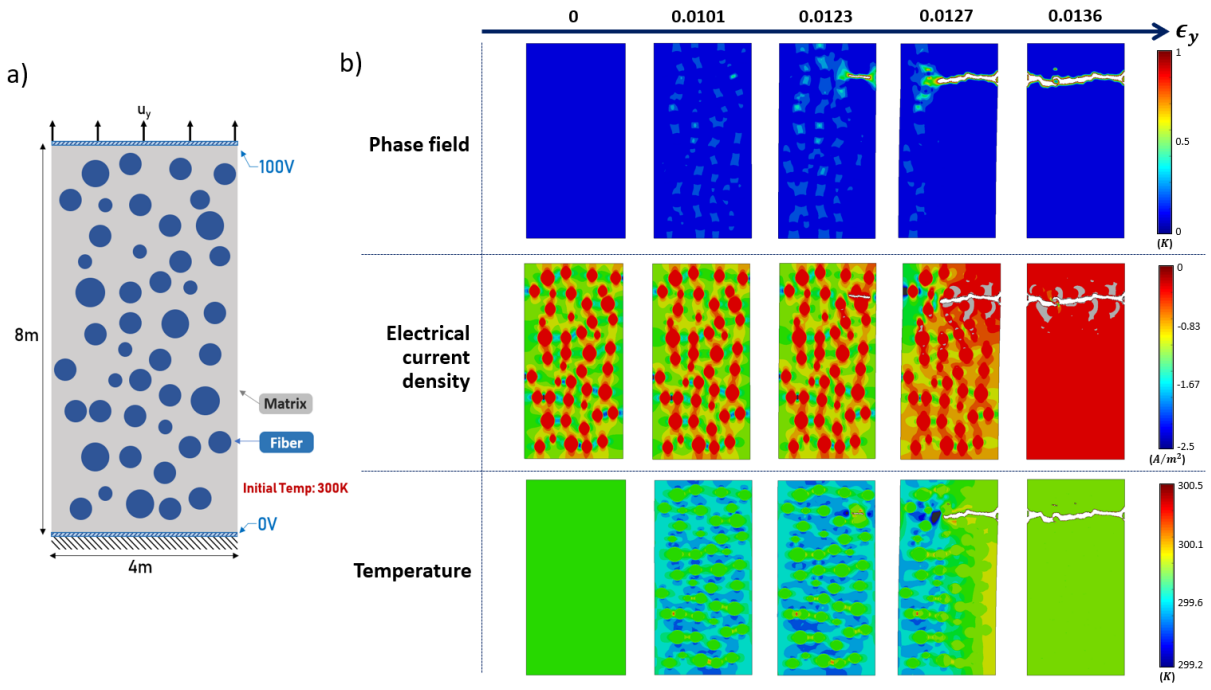

Figure 7. Multiphysics simulation on 2D GFRP specimen. (a) Virtual specimen geometry and the tensile simulation conditions. (b) Mechanical, electrical and thermal response of the GFRP during the tensile simulation.

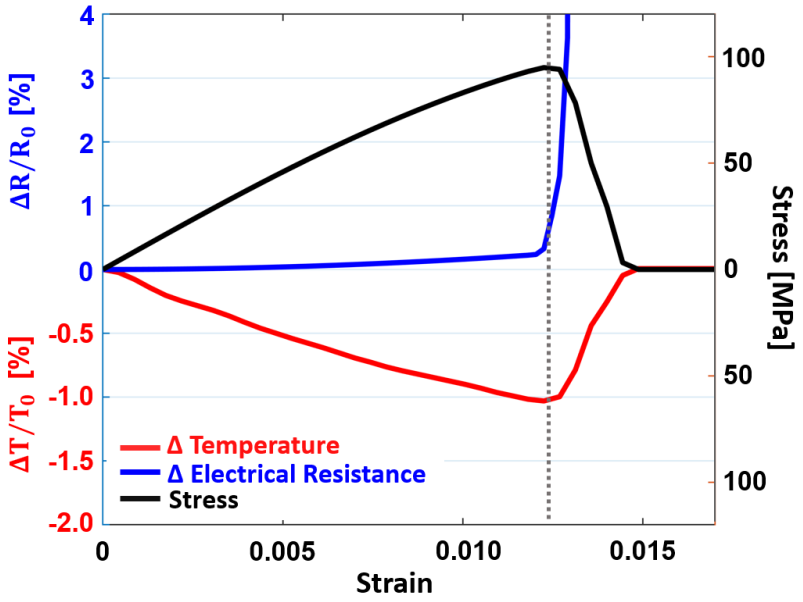

Figure 8. 3-channel response of the 2D GFRP specimen during the tensile simulation.

References

1 Chang, f.-k. (1998). "Structural Health Monitoring: A Summary Report on the First Stanford Workshop on Structural Health Monitoring, September 18-20, 1997." 13.

2 Abdo, M. (2014). Structural Health Monitoring, History, Applications and Future. A Review Book.

3 Kessler, S. S. (2002). Piezoelectric-based in-situ damage detection of composite materials for structural health monitoring systems, Massachusetts Institute of Technology.

4 Fernández Sánchez-Romate, X. X., et al. (2017). "Carbon Nanotube-Doped Adhesive Films for Detecting Crack Propagation on Bonded Joints: A Deeper Understanding of Anomalous Behaviors." ACS Applied Materials & Interfaces 9(49): 43267-43274.

5 Matos, M. A. S., et al. (2018). "Predictions of the electro-mechanical response of conductive CNT-polymer composites." Journal of the Mechanics and Physics of Solids 114: 84-96.

6 Thostenson, E. T. and T.-W. Chou (2006). "Carbon Nanotube Networks: Sensing of Distributed Strain and Damage for Life Prediction and Self Healing." Advanced Materials 18(21): 2837-2841.

7 Gao, L., et al. (2009). "Coupled carbon nanotube network and acoustic emission monitoring for sensing of damage development in composites." Carbon 47(5): 1381-1388.

8 Ku-Herrera, J. J., et al. (2016). "Self-Sensing of Damage Progression in Unidirectional Multiscale Hierarchical Composites Subjected to Cyclic Tensile Loading." Sensors (Basel, Switzerland) 16(3): 400.

9 Libonati, F. and L. Vergani (2013). "Damage assessment of composite materials by means of thermographic analyses." Composites Part B: Engineering 50: 82-90.

10 Vergani, L., et al. (2013). "A review of thermographic techniques for damage investigation in composites." Frattura ed Integrità Strutturale 8(27).

11 Murakami, Y. and M. Endo (1994). "Effects of defects, inclusions and inhomogeneities on fatigue strength." International Journal of Fatigue 16(3): 163-182.

12 Murakami, Y. and T. Endo (1980). "Effects of small defects on fatigue strength of metals."

International Journal of Fatigue 2(1): 23-30.

13 Libonati, F., et al. (2011). "Fatigue behaviour of a GFRP laminate by thermographic measurements." Procedia Engineering 10: 3518-3527.

14 Colombo, C. (2012). "Fatigue damage in GFRP." International Journal of Structural Integrity 3(4): 424-440.

15 Sánchez-Romate, X. F., et al. (2016). "Novel approach to percolation threshold on electrical conductivity of carbon nanotube reinforced nanocomposites." Rsc Advances 6(49): 43418-43428.

16 ASTM International. (2017). “D3039/D3039M-17 Standard Test Method for Tensile Properties of Polymer Matrix Composite Materials.”

17 Jirathearanat, S., et al. (2004). "Hydroforming of Y-shapes—product and process design using FEA simulation and experiments." Journal of Materials Processing Technology 146(1): 124-129.

18 Fu, M. W., et al. (2008). "Design solution evaluation for metal forming product development." The International Journal of Advanced Manufacturing Technology 38(3): 249-257.

19 Spatschek, R., et al. (2006). "Phase Field Modeling of Fast Crack Propagation." Physical Review Letters 96(1): 015502.

20 Duarte, C. A., et al. (2001). "A generalized finite element method for the simulation of three-dimensional dynamic crack propagation." Computer Methods in Applied Mechanics and Engineering 190(15): 2227-2262.

21 Kim, S. and S. Ryu (2017). "Effect of surface and internal defects on the mechanical properties of metallic glasses." Scientific Reports 7(1): 13472.

22 Lee, S., et al. (2019). "Atomistic simulation study on the crack growth stability of graphene under uniaxial tension and indentation." Meccanica.

23 Msekh, M. A., et al. (2015). "Abaqus implementation of phase-field model for brittle fracture." Computational Materials Science 96: 472-484.

24 Molnár, G. and A. Gravouil (2017). "2D and 3D Abaqus implementation of a robust

staggered phase-field solution for modeling brittle fracture." Finite Elements in Analysis and Design 130: 27-38.

25 Jeong, H., et al. (2018). "Phase field modeling of crack propagation under combined shear and tensile loading with hybrid formulation." Computational Materials Science 155: 483-492.

26 Coggon, J. H. (1971). "Electromagnetic and electrical modeling by the finite element method." Geophysics 36(1): 132-155.

27 Lewis, R. W., et al. (1996). The Finite Element Method in Heat Transfer Analysis, Wiley.

28 Pitarresi, G. and E. A. Patterson (2003). "A review of the general theory of thermoelastic stress analysis." The Journal of Strain Analysis for Engineering Design 38(5): 405-417.

29 Wallenberger, F. T., et al. (2001). “Glass Fibers” Composites. D. B. Miracle and S. L. Donaldson, ASM International. 21: 0.

30 Ciba Specialty Chemicals (1998). “Hot curing epoxy system based on Araldite LY556 / Hardener HY917 / Accelerator DY070”, MATRIX SYSTEMS FOR INDUSTRIAL COMPOSITES – DATA SHEET

31 Hashin, Z. (1986). "Analysis of stiffness reduction of cracked cross-ply laminates." Engineering Fracture Mechanics 25(5): 771-778.

32 Talreja, R. (1985). "Transverse Cracking and Stiffness Reduction in Composite Laminates." Journal of Composite Materials 19(4): 355-375.